Title

Thermally switchable, crystallizable oil and silicone composite adhesives for skin-interfaced wearable devices.

Journal

Science Advances, 8(23)

Authors

Jinkins, Katherine
Li, Shupeng
Arafa, Hany
et al.

Publication Date

2022-06-10

DOI

10.1126/sciadv.abo0537

Peer reviewed

ENGINEERING

Thermally switchable, crystallizable oil and silicone composite adhesives for skin-interfaced wearable devices

Katherine R. Jinkins[1]†, Shupeng Li[2,3,4]†, Hany Arafa[1,5], Hyoyoung Jeong[1], Young Joong Lee[1], Changsheng Wu[1], Elizabeth Campisi[1], Xinchen Ni[1], Donghwi Cho[1,6], Yonggang Huang[2,3,4]*, John A. Rogers[1,4,5,7,8]*

Continuous health monitoring is essential for clinical care, especially for patients in neonatal and pediatric intensive care units. Monitoring currently requires wired biosensors affixed to the skin with strong adhesives that can cause irritation and iatrogenic injuries during removal. Emerging wireless alternatives are attractive, but requirements for skin adhesives remain. Here, we present a materials strategy enabling wirelessly triggered reductions in adhesive strength to eliminate the possibility for injury during removal. The materials involve silicone composites loaded with crystallizable oils with melting temperatures close to, but above, surface body temperature. This solid/liquid phase transition occurs upon heating, reducing the adhesion at the skin interface by more than 75%. Experimental and computational studies reveal insights into effects of oil mixed randomly and patterned deterministically into the composite. Demonstrations in skin-integrated sensors that include wirelessly controlled heating and adhesion reduction illustrate the broad utility of these ideas in clinical-grade health monitoring.

INTRODUCTION

For many patients, medical treatments rely upon continuous health monitoring to ascertain changes to physiological status and to guide clinical decision making. Current state-of-the-art technologies for such purposes require biosensors that adhere to the skin and connect to external hardware for data acquisition, processing, and storage. These wired platforms yield high-quality data, but with substantial disadvantages for vulnerable patients, particularly those in neonatal and pediatric intensive care unit (NICU and PICU) facilities. Wires attached to infants restrict their natural movements, they complicate basic operations in care such as bathing, changing diapers, and feeding, and they limit opportunities for skin-to-skin bonding with parents (i.e., kangaroo care) (*1*). In addition, injuries associated with removal of medical adhesives occur frequently in patients with thin and fragile skin, particularly those in the NICU and PICU (*2*, *3*) and the elderly (*4*).

Soft, wireless electronic devices offer an emerging, alternative method for continuous monitoring, without many of the drawbacks of conventional approaches, especially for vulnerable populations. The most advanced devices are exceptionally thin and stretchable, mimicking the mechanical properties of the skin, with capabilities for capturing important health metrics at clinical-grade quality, including heart rate and variation, respiration rate, blood oxygenation levels, pulse wave velocity, and skin temperature (*5*). These devices use near-field communication (NFC) for power and communication, thereby eliminating the need for batteries, and their associated bulk and weight. These skin-like devices allow for the use of mild adhesives and, in some cases, no adhesives, thereby reducing the risks for skin injury upon device removal. A disadvantage of the NFC approach is that it restricts the operating range to a distance of less than ~1 m from the transmission antenna. In addition, requirements for radio-frequency electronics and reliable sources of wall-plug power prevent practical use in low-resource areas of the globe.

Related classes of devices built using Bluetooth technology and small, rechargeable batteries, overcome these limitations (*6*). The batteries, however, increase the thicknesses and masses of the devices, such that enhanced adhesives must be used, along with associated risks to the skin. These circumstances motivate the development of schemes for reducing adhesion immediately before removal as a means to eliminate the potential for injury. Classes of materials that can be applied to the skin in a high adhesion state and then removed safely after triggering a transition to a lower adhesion state may provide a solution. Previously reported strategies rely on mechanical (*7*, *8*), electromagnetic (*9*, *10*), fluidic (*11*, *12*), and thermal (*13*, *14*) mechanisms for modulating the adhesion strength (*15*). A simple but effective example in wireless health monitoring systems exploits hydrogel adhesives and "holey" device architectures. In these architectures, warm water introduced at the skin/hydrogel adhesive interface through the holes leads to swelling of the hydrogel and associated marked reductions in the strength of adhesion to the skin (*16*). Practical disadvantages are in the need to carefully apply water to the device and in the relatively slow kinetics of swelling.

This paper introduces a strategy that enables fast, wirelessly triggered reductions in adhesion using a thermally switchable composite silicone material. Tailored formulations and structures exhibit robust adhesion to the skin until a thermally induced phase transition reduces the strength of adhesion to enable safe and gentle device removal. The system exploits soft silicone polymers as matrices to support dispersions of common crystallizable oils used in commercial skin care products. The melting points of the oils are close to, but slightly above, normal temperatures at the surface of the skin, thereby preventing unwanted reductions in adhesion during use

[1]Querrey Simpson Institute for Bioelectronics, Northwestern University, Evanston, IL 60208, USA. [2]Department of Mechanical Engineering, Northwestern University, Evanston, IL 60208, USA. [3]Department of Civil and Environmental Engineering, Northwestern University, Evanston, IL 60208, USA. [4]Department of Materials Science and Engineering, Northwestern University, Evanston, IL 60208, USA. [5]Department of Biomedical Engineering, Northwestern University, Evanston, IL 60208, USA. [6]Thin Film Materials Research Center, Korea Research Institute of Chemical Technology, Yuseong, Daejeon 34114, Republic of Korea. [7]Department of Chemistry, Northwestern University, Evanston, IL 60208, USA. [8]Department of Neurological Surgery, Feinberg School of Medicine, Northwestern University, Chicago, IL 60611, USA.
*Corresponding author. Email: y-huang@northwestern.edu (Y.H.); jrogers@northwestern.edu (J.A.R.)
†These authors contributed equally to this work.

and allowing the switching process to occur without excessive thermal exposure to the skin. Experimental measurements and modeling results define the effects of oil loading and oil chemistry on adhesion as a function of temperature. Demonstrations with various wireless, skin-integrated devices, including those with programmable heating units, highlight practical application possibilities of the materials and mechanisms introduced here.

RESULTS

The approach exploits a thin composite film placed between the skin and the wearable device, as illustrated in Fig. 1 (A and B). This film provides robust adhesion at temperatures below those slightly above the natural temperature of the skin to allow reliable coupling to the body during operation. Mild heating to increase the temperature by a few degrees Celsius substantially and rapidly reduces the strength of adhesion between this film and the surface of the skin to eliminate the risk of discomfort or iatrogenic injuries to the skin during device removal, of particular importance to vulnerable patients with fragile skin, such as neonates (*17*) and the elderly (*18*). This thermally switchable adhesive supports a single cycle of use and separately bonds to the wearable device using an adhesive (Fig. 1B), thereby enabling the adhesive to be removed after use and reducing the probability of contamination between patients. In addition, the switching temperature of the adhesive lies well below the thresholds for skin damage even for infants, as described in detail subsequently (*19*, *20*). The composite combines a crystallizable oil distributed in a silicone matrix (*21*) as randomly distributed crystallites through

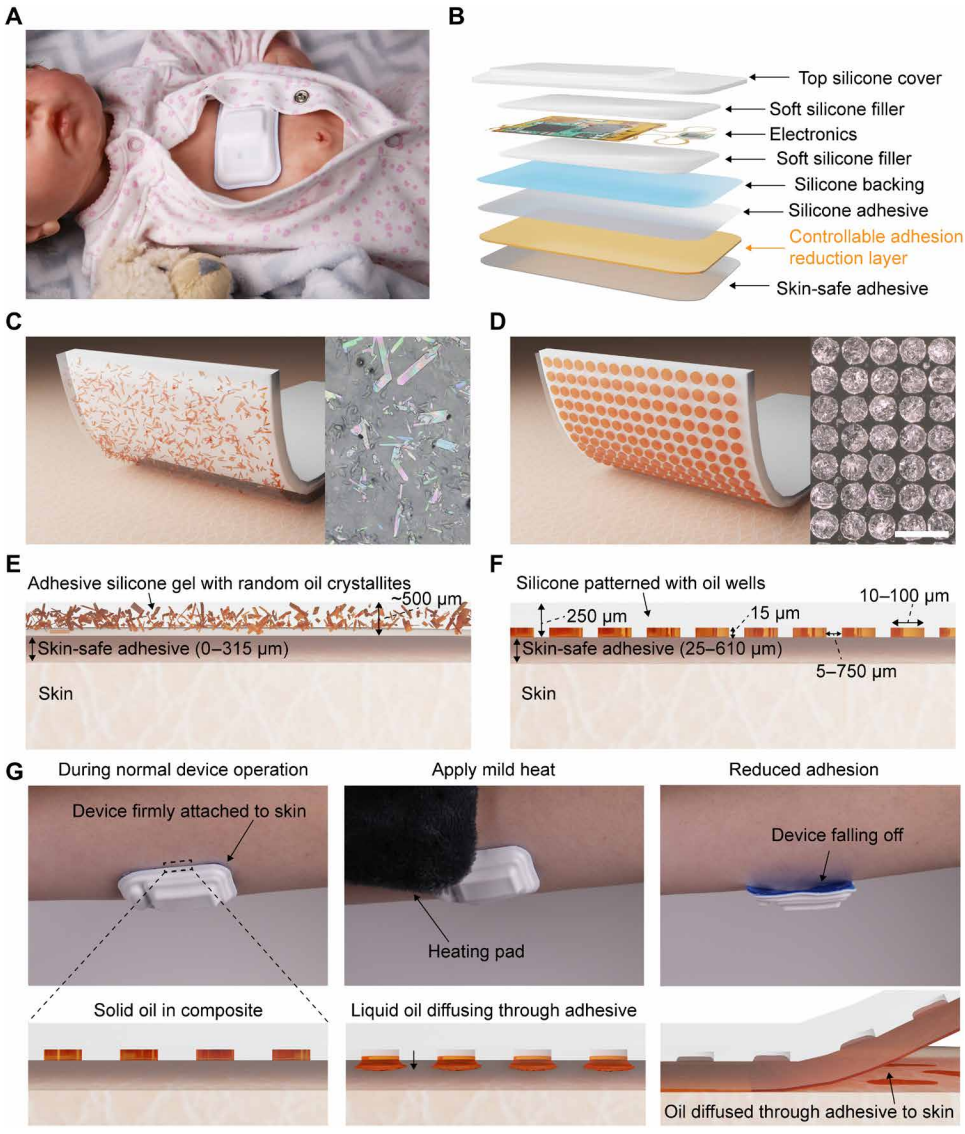

Fig. 1. Design of a thermally switchable adhesive silicone composite for use in skin-mounted devices. (**A**) Life-sized neonate doll wearing an electronic device for capturing biosignals. (**B**) Layer with switchable adhesion strength integrated in a wearable device architecture. Random oil crystallite (**C**) and patterned oil well (**D**) composites for thermally switchable adhesives. Scale bar in optical image (D) is 100 μm and applies to optical images in both (C) and (D). (**E** and **F**) Cross-sectional schematic illustrations with dimensions of random crystallite and patterned well architectures, respectively. (**G**) Process flow for use of wearable devices that integrate a thermally switchable adhesive layer.

the thickness of the material (Fig. 1, C and E) or as patterned, circular disks (Fig. 1, D and F) near the surface. In both cases, a thin overcoat of adhesive silicone gel (e.g., interface layer) forms the bonding interface to the skin. The oils explored in this work include fatty alcohols (1-pentadecanol and 1-hexadecanol) and linear alkanes (*n*-docosane and eicosane), chosen with melting temperatures slightly above those that characterize the natural temperature of the skin surface across various regions of the body (33° to 37°C) (*22*). These oils, as well as the silicone polymers, are biocompatible and widely used in skincare products (*23*–*26*), drug delivery systems (*27*–*36*), and skin bandage materials (*37*–*39*).

Figure 1G shows pictures and schematic illustrations of the operating principles applied with a representative skin-interfaced wearable device. During normal use, the oil remains in a solid state and the device adheres robustly to the skin. Mild heating causes the oil to melt, thereby allowing it to diffuse in a liquid state through the silicone adhesive layer to the interface with the skin. During oil diffusion, the adhesive silicone layer collapses into the void spaces or the now empty wells. Accumulation of liquid oil at the skin interface markedly reduces the strength of adhesion between the device and the skin. In this state, the device can be removed with exceptionally low applied peel forces, in some cases, within the range of those provided by gravity.

Characterization of the morphology and adhesive properties of random composites

Systematic studies of materials in the random oil crystallite architecture reveal the effects of the volume fraction and type of oil in the composite, the properties of the interface layer, and the switching temperature. Formation of the composite involves mixing the oil in its liquid state into an uncured adhesive silicone matrix, spin-coating the resulting mixture, and then cooling to and curing at room temperature to yield a solid film (Fig. 2A). The samples studied here involve crystallites of oils that include 1-pentadecanol (TCI America), 1-hexadecanol (Thermo Fisher Scientific), *n*-docosane (Thermo Fisher Scientific), and eicosane (Thermo Fisher Scientific) and commercial formulations of adhesive silicone gels (Ecoflex gel, Smooth-On or Silbione gel RT 4717, Elkem Silicones, referred to as silicone gel 1 and 2, respectively). The elastic modulus increases and optical transmittance decreases with increasing oil loading (figs. S1 and S2). The effective thermal conductivity of the adhesives also slightly increases with increasing oil loading (fig. S3).

A modified T-peel test, where the adhesive composite adheres to a silicone skin replica (fig. S4) and peeling occurs at a constant velocity (0.5 mm s^{-1}), yields force measurements as a function of displacement. The adhesion energies are twice the saturated peeling force divided by the sample width (*40*, *41*). The Materials and Methods discusses details of this measurement process.

Figure 2B shows the dependence of the adhesion energy on the weight fraction (wt %) of oil at room temperature (23°C) and above the melting point of the oil for composites of 1-pentadecanol (T_m = 42° to 46°C) in silicone gel 1. At room temperature, increasing the amount of oil from 5 to 20 wt % leads to a slight decrease in adhesion from 15.0 ± 3.3 to 11.6 ± 2.1 J m^{-2}. The adhesion decreases from 11.6 ± 2.1 J m^{-2} at 23°C to 3.0 ± 0.9 J m^{-2} at 45°C for composites with 20 wt % oil.

Experiments indicate similar trends for composites of 1-pentadecanol in silicone gel 2, an adhesive silicone with higher initial adhesion (44.6 ± 4.8 J m^{-2}) than silicone gel 1 (12.5 ± 2.5 J m^{-2}) (fig. S5). These data can be described using analytical models that consider the surface area of the composites occupied by the oil (as opposed to adhesive silicone) and the adhesive properties of each material when the oil is in solid (23°C) and/or liquid (at T_m and T_m + 5°C) forms. Here, the adhesion energy γS can be related to the product of the surface contact area S and work of adhesion γ (with the attached material). For a composite of gel and (solid) oil, γ can be described in terms of the area fraction f of the oil by

$$\gamma = f\gamma_{oil} + (1 - f)\gamma_{gel} \quad (1)$$

where γ_{oil} and γ_{gel} are the work of adhesion (with the attached skin replica) for the oil and gel, respectively. For oil randomly distributed in the gel, on the average, the area fraction is the same as the volume fraction, such that both can be denoted by f. The volume fraction f is related to the weight fraction (wt %) by $f = \frac{wt\%}{wt\% + (\rho_{oil}/\rho_{gel})(1 - wt\%)}$, where ρ_{oil} and ρ_{gel} are the mass density of oil and gel, respectively.

The (solid) oil melts as the temperature exceeds its melting point, and the liquid oil flows into the interface between the gel and the skin, such that the area fraction of liquid oil, f_{liquid}, increases with temperature and is no longer equal to the volume fraction f of solid oil. For the limits of no oil (f = 0) and complete saturation of oil (f = 1), f_{liquid} = 0 and 1, respectively. Consistent with these limits, a power law relationship can be assumed $f_{liquid} = f^{\alpha}$, where α is between 0 and 1 (such that $f_{liquid} \geq f$) and decreases as with increasing occupation of liquid oils at the interface. In addition, α also depends on the temperature (Fig. 2C), types of adhesive silicon gels (Fig. 2B and fig. S5), and oils (fig. S6 and table S2). With this simple model, which avoids a complex analysis of the dependence of interfacial debonding on invasion of liquid oil, the work of adhesion becomes

$$\gamma = f^{\alpha}\gamma_{liquid\_oil} + (1 - f^{\alpha})\gamma_{gel} \quad (2)$$

where γ_{liquid_oil} is the work of adhesion for the liquid oil.

Using material densities and adhesion energies for the oil and silicone materials (table S1), analytic calculations performed using this model correspond well with experimental data. Fitting the data when the oil is melted (dashed line in Fig. 2B) yields α = 0.14 for 1-pentadecanol in silicone gel 1. By comparison, composites of 1-pentadecanol in silicone gel 2 exhibit a larger α value of 0.33, likely due to the higher initial adhesion (table S2).

Figure 2C summarizes the effect of temperature on the adhesion for this random oil crystallite design. For the case of 20 wt % 1-pentadecanol in silicone gel 1, the adhesion remains constant with temperature across a relevant range for values (23° to 42°C) below the melting point of the oil (11.2 ± 1.7 J m^{-2}). At 45°C, near the melting point of the oil, the adhesion sharply decreases to a value (3.0 ± 0.9 J m^{-2}) that does not markedly change with additional increases in temperature (average adhesion above 45°C is 3.3 ± 0.2 J m^{-2}). The results are consistent with a mechanism for thermal switching between high and low adhesion states.

Linear alkanes represent additional options for the crystallizable oils. The adhesion energies as a function of oil weight fraction (at room temperature, i.e., when the oil is solid) exhibited by the fatty alcohols, as compared to the linear alkanes, more closely match those predicted at room temperature by the model described previously (fig. S6). For example, composites of *n*-docosane (T_m = 42° to 45°C) in silicone gel 1 exhibit adhesion energies at room temperature that

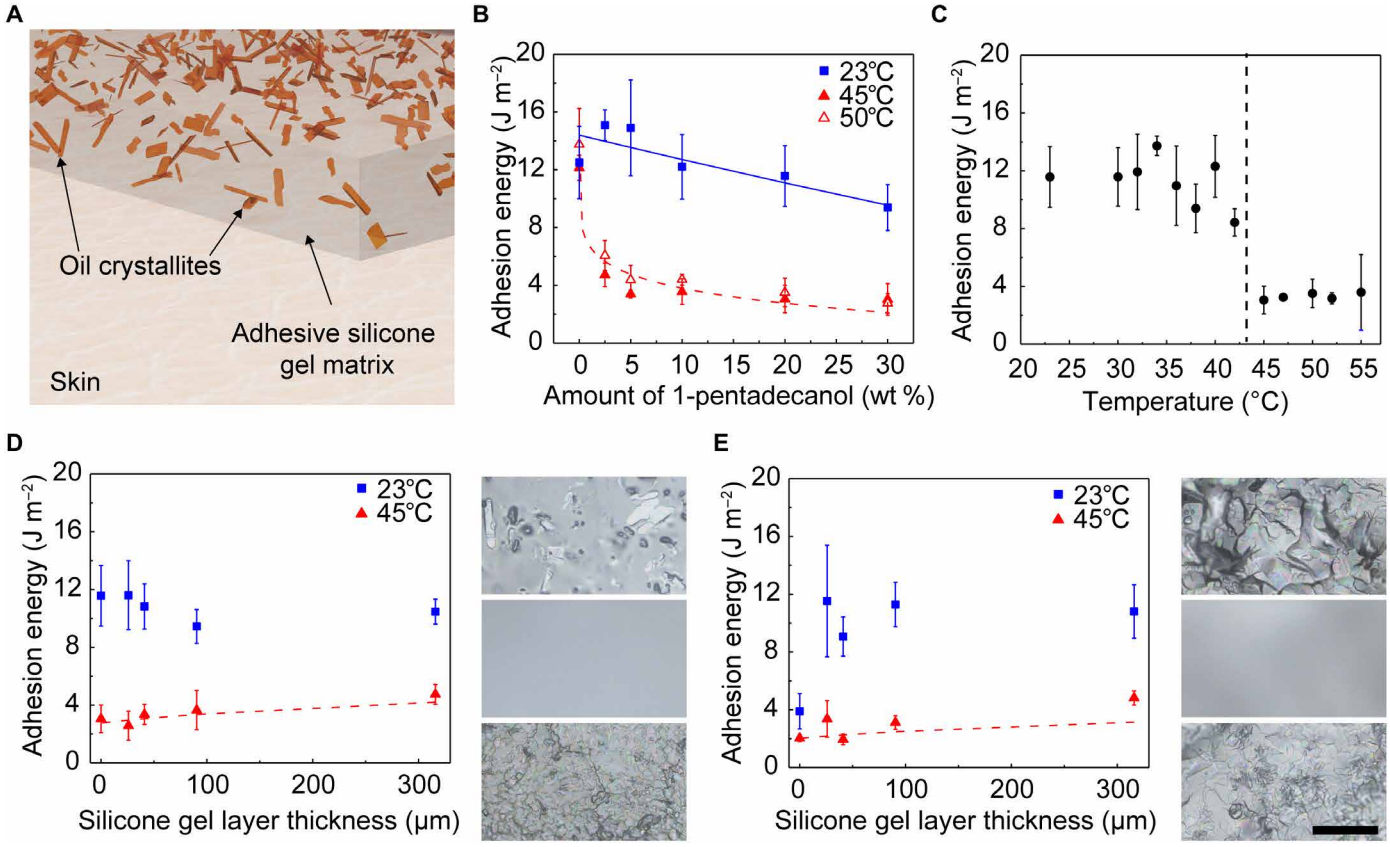

Fig. 2. Characterization of random oil crystallite/silicone composites for thermally switchable adhesives. (**A**) Schematic illustration of random oil crystallite architecture. (**B**) Adhesion energy versus amount of 1-pentadecanol in adhesive silicone (silicone gel 1) at 23°, 45°, and 50°C. Solid and dashed lines correspond to an analytic model. (**C**) Adhesion energy versus temperature for 20 wt % 1-pentadecanol in silicone gel layer 1. (**D** and **E**) Adhesion energy versus thickness of silicone gel 1 layer on composites of 20 wt % 1-pentadecanol and *n*-docosane, respectively, in silicone gel 1 measured at 23° and 45°C. Dashed lines correspond to analytic model. At the right of each plot are optical images of the initial composite (top), after coating with 90 μm of silicone gel 1 (middle), and after heating the gel-coated composite (bottom). Scale bar is 100 μm and applies to all optical images in (D) and (E). Each data point and error bar are calculated from five different samples ($n = 5$).

notably decrease from 9.5 ± 2.2 to 3.9 ± 1.2 J m^{-2} with increasing oil weight fraction from 5 to 20 wt % (fig. S6C). These unexpected trends arise largely from differences in the morphologies of the oil crystallites and the associated surface roughness (figs. S7 and S8A). For all oils examined in silicone gel 1, the α values (calculated when the oil is melted) are similar (0.1 to 0.14; table S2).

An interfacial layer of adhesive silicone (silicone gel 1) added between the composite and the skin shown in Fig. 2A (schematic illustration of coated composite shown in Fig. 1C) can planarize any roughness on the surface of the composite (fig. S8B). This adhesive silicone demonstrates excellent adhesion at room temperature (0 wt % data points shown in Fig. 2B and table S1). Results of studies of the effect of the interface layer appear in Fig. 2 (D and E). For composites of 20 wt % 1-pentadecanol in silicone gel 1, the adhesion is similar regardless of the thickness of the adhesive layer (Fig. 2D). At 45°C, the adhesion increases slightly with increasing interface layer thickness, 3.0 ± 1.0 to 4.7 ± 0.7 J m^{-2} at 0 and 315 μm, respectively. For composites of *n*-docosane in silicone gel 1, the adhesion at room temperature increases markedly upon the addition of an adhesive interface layer from 3.9 ± 1.2 to 10.8 ± 1.8 J m^{-2} at 0 and 315 μm (Fig. 2E), consistent with a planarizing effect of the interfacial layer. Similar to 1-pentadecanol, the adhesion at 45°C also increases with thickness of the interface layers from 2.0 ± 0.2 to 4.8 ± 0.5 J m^{-2} for thicknesses of 0 and 315 μm, respectively.

Analytic models described previously can be modified to include the effects of the interfacial adhesive layer. Adding this layer, with thickness $h_{interface}$, between the composite and skin, modifies the volume fraction at the interface to $f_{interface} = \frac{h}{h + h_{interface}} f$, where h is the thickness of the composite. According to this form, $f_{interface}$ approaches f as $h_{interface}$ approaches zero. The work of adhesion below the melting temperature is $\gamma = \gamma_{gel}$, and the work of adhesion above the melting temperature is derived by replacing f into $f_{interface}$ in Eq. 2

$$\gamma = \left(\frac{h}{h + h_{interface}} f\right)^{\alpha} \gamma_{liquid} + \left[1 - \left(\frac{h}{h + h_{interface}} f\right)^{\alpha}\right] \gamma_{gel} \quad (3)$$

Using the same α from table S2 determined for 1-pentadecanol and *n*-docosane, this model matches the experimental data well (Fig. 2, D and E) without any parameter fitting. Optical images from 1-pentadecanol and *n*-docosane composites initially (top), after coating with the adhesive interface layer (middle), and after heating at 45°C, confirm that the embedded oil diffuses through the adhesive interfacial layer as the main mechanism for reductions in adhesion (Fig. 2, D and E).

Characterization of the morphology and adhesive properties of deterministic composites

As an alternative to a uniform, random distribution of oil crystallite throughout the thickness of the composite, patterned architectures of oil confined to the surface can be considered. Here, a process of discontinuous dewetting of heated liquid oil onto the surface of a silicone film with arrays of cylindrical features of bas relief, followed by cooling leaves circular disks of solid oil (*42*, *43*) at the surface. As the liquid travels across the mold, it pins on the edge of the wells due to the structural heterogeneity. While the bulk liquid continues across the unpatterned regions, the pinned contact line remains in place until a drop ruptures from the bulk liquid, thereby filling the well. The Materials and Methods includes details. This scheme offers an attractive route to uniformly and rapidly fill wells of different diameters (1-pentadecanol filled wells with diameters of 100, 50, and 10 μm shown in Fig. 3B) and different spacings (Fig. 3B, middle panel inset) over large areas, without defects. Composites with dense arrays of wells near the outer perimeter (fig. S9) enhance peeling from the edges of devices, minimizing strain on the skin. An overcoat of silicone (silicone gel 1) defines an interfacial adhesive layer used to attach the composites to the skin (as shown in Fig. 1F), similar to that used with the random composite materials described previously (shown in Figs. 1C and 2, D and E). Because of the roughness of the filled oil wells, the adhesion energy of the composites increases with increasing interfacial adhesive layer thickness. The adhesion energy ceases to increase with thickness above 315 μm (fig. S10). The elastic modulus of the patterned well composites increases and the optical transmittance decreases when the wells are filled with oil, as compared to empty (figs. S11 and S12). The effective thermal conductivity slightly increases after filling the wells with oil (fig. S13).

Data presented in Fig. 3 (C and D) summarize the effects of well diameter and spacing on the adhesion properties. At 23°C, all composites exhibit similar adhesion, regardless of spacing or diameter, due to the dominating role of the interfacial layer of silicone gel 1 that coats the oil wells (Fig. 3, C and D). For wells with the same diameter (50 μm), decreasing the well spacing from 750 to 10 μm also reduces adhesion at 50°C from 9.2 ± 1.7 to 1.8 ± 0.6 J m^{-2} (Fig. 3C). For a given edge-to-edge spacing of 10 μm, the adhesion at 50°C decreases slightly from 3.4 ± 0.9 to 1.7 ± 0.4 J m^{-2}, with increasing well diameter from 10 and 100 μm (Fig. 3D).

For these deterministically patterned oil wells, the area fraction f_{well} can be directly used to replace f in Eq. 2

$$\gamma = f_{well}^{\alpha}\gamma_{liquid\_oil} + (1 - f_{well}^{\alpha})\gamma_{gel} \quad (4)$$

The area fraction, in this case, is the total area covered by wells divided by the total area, where the total well area is a function of both the well diameter and spacing. Using $\alpha = 0.14$ for 1-pentadecanol (table S2), analytical calculations performed both as a function of well spacing (Fig. 3C) and diameter (Fig. 3D) correspond well with experiment.

Independent of the well diameter, spacing, or oil type (oils chosen because of melting temperatures), for the cases examined here, the area covered by the wells largely determines the adhesion for temperatures above the melting point of the oil (Fig. 3E). For example, the adhesion decreases from 7.9 ± 1.2 to 1.5 ± 0.6 J m^{-2} at 2 and 35% of the total area occupied by wells, respectively, for 1-pentadecanol and from 8.5 ± 1.5 to 1.2 ± 0.6 J m^{-2} for *n*-docosane. Previously determined α values for 1-pentadecanol and *n*-docosane (table S2) yield analytical results that match the experimental data well (Fig. 3E) without any parameter fitting.

Three-dimensional (3D) confocal reflectance microscopy confirms the oil configuration within the wells before (Fig. 3F) and after (Fig. 3G) heating. Before heating, the silicone gel interface layer covers uniformly filled oil wells. After heating for 60 s, the oil diffuses through the interface layer and reduces adhesion at the skin. Measurements of diffusion coefficients of oil in silicones yield approximate time scales for oil diffusion, which are similar to those observed qualitatively in these images (fig. S14 and note S1). When coated with a layer of silicone gel, the oil wells and adhesives demonstrate excellent stability and maintain adhesion switching properties over a period of 6 months, as investigated here (fig. S15).

Skin-interfaced biosensors attached using thermally switchable adhesives

Uses with three wireless, skin-interfaced devices (Fig. 4A) demonstrate these thermally switchable adhesives in a range of health monitoring applications: (i) a near–infrared (IR) spectroscopy (NIRS) system for assessing brain function and oxygenation (*44*), (ii) a mechano-acoustic (MA) sensor for motion tracking and monitoring vibrations associated with processes within the body (*6*, *45*, *46*), and (iii) an electrocardiogram (ECG) monitor for assessing cardiac health (*6*). In all cases, thermally switchable adhesives bond these devices to the body during operation, demonstrating good mechanical, electrical, optical, and thermal coupling to the skin.

Measurements of reflectance-mode photoplethysmograms (PPGs) captured from the forehead at red (740 nm) and IR (850 nm) wavelengths, sampled at 25 Hz, confirm the operation of the NIRS device (Fig. 4B). Measured with the patient at rest, eight cardiac cycles occur within 10 s, corresponding to a heart rate of 48 beats/min (Fig. 4B). Windows cut in the adhesive layer at each light-emitting diode and photodetector enable measurement in a manner that avoids any effect of the adhesive on the signal. The MA device mounts on the suprasternal notch to perform wide bandwidth accelerometry across three axes. These data correspond not only to bulk, low-frequency motions of the body but also to subtle, high-frequency vibrations at the surface of the skin that correlate to cardiopulmonary activity and other physiological processes. Figure 4C shows representative data from a healthy adult individual participating in a series of activities. Accelerations in the direction perpendicular to the surface of the skin (z) show cycles of expansion and contraction of the chest as normal respiratory activity during the first 25 s and last 50 s of the data. The data also include signatures of other events during the measurement period, including holding breath (25 to 40 s), talking (40 to 65 s), drinking water (75 to 100 s), and jumping (140 to 163 s) as examples. Cardiac activity (Fig. 4D) and respiration rate (Fig. 4E) extracted from data shown in Fig. 4C confirm that the quality of the measurements is indistinguishable from that collected with devices that use conventional adhesives. Skin temperature measurements from the MA device attached to the body using switchable adhesives match measurements performed with conventional adhesives (fig. S16). Videos demonstrate the enhanced removal of the MA device attached with thermally switchable adhesives (movies S1 and S2). Last, temperature switchable adhesives can replace the bulk (i.e., nonconductive) adhesive used to attach the ECG device to the skin. Openings in the thermally switchable adhesive allow the use of conductive hydrogel adhesives (KM 40A, Katecho) at the electrode locations. The resulting data signals are comparable to those

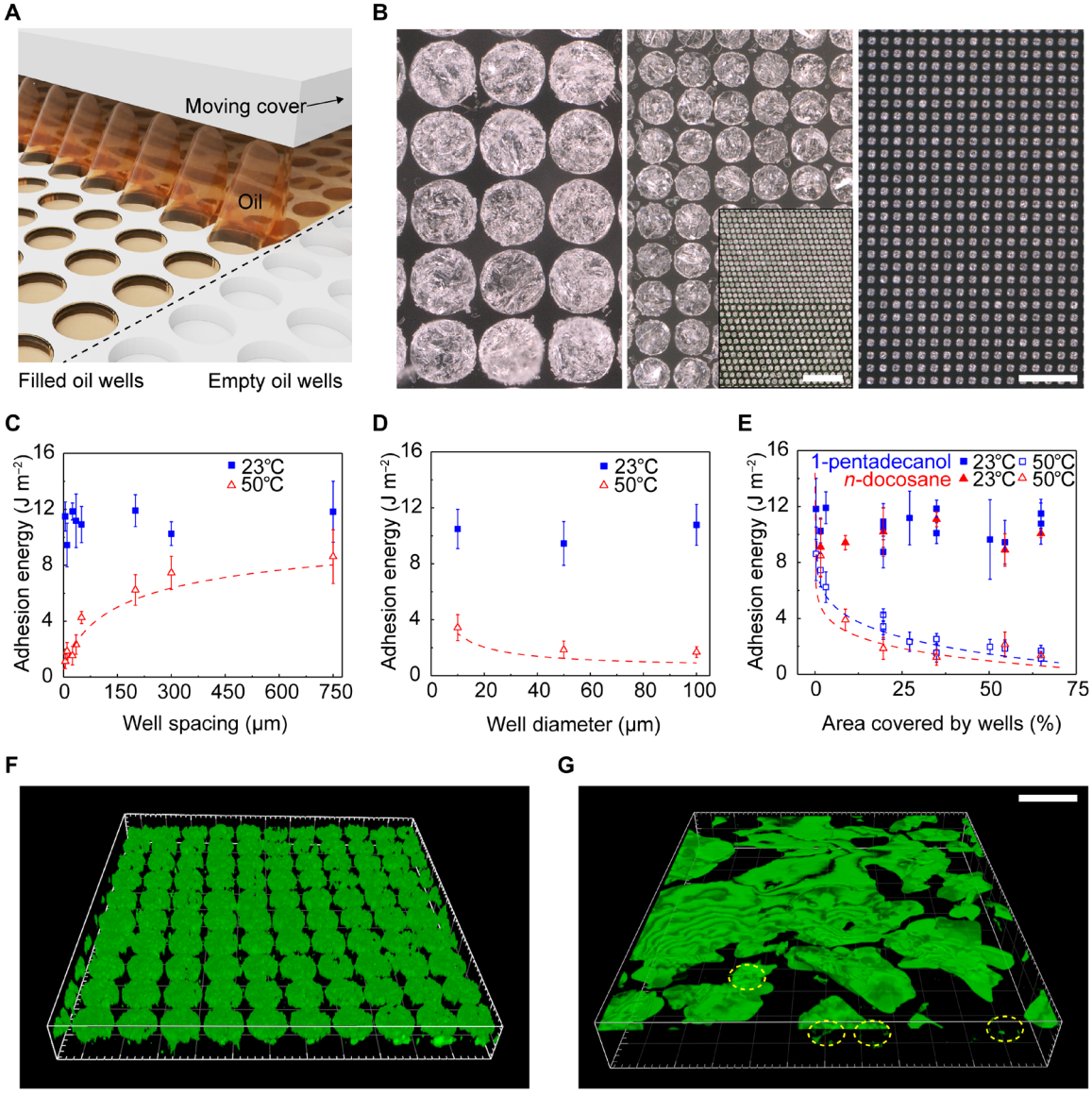

Fig. 3. Characterization of patterned oil well/silicone composites for thermally switchable adhesives. (**A**) Schematic illustration of the discontinuous dewetting procedure for filling patterned silicone wells with oil. (**B**) Optical images of silicone wells (diameters, 100, 50, and 10 μm) filled with 1-pentadecanol. Scale bar is 100 μm and applies to all larger panels. Middle panel inset: Optical image of 50-μm-diameter wells with different spacings (10 and 35 μm). Scale bar is 500 μm. (**C**) Effect of well spacing at a set well diameter (50 μm) and (**D**) effect of well diameter at a set well spacing (10 μm) on adhesion energy of 1-pentadecanol composites. Blue squares and open red triangles are data measured at 23° and 50°C, respectively. (**E**) All data in (C) and (D) combined, in addition to data from *n*-docosane composites, show that the total oil well area defines the adhesion energy, independent of well diameter, spacing, or oil type (blue squares, 1-pentadecanol; open red triangles, *n*-docosane). Closed and open data points are measured at 23° and 50°C, respectively. For certain samples, the area covered by oil is the same (e.g., samples with well spacing and a diameter of 100 μm exhibit the same oil area as samples with spacing and a diameter of 50 μm), yielding data points that appear to overlap at the same *x* value. (**F** and **G**) 3D laser confocal reflectance imaging of filled oil wells (diameter, 50 μm; spacing, 10 μm) covered with a layer (100 μm) of silicone gel 1 before (F) and after (G) melting. After heating (50°C for 60 s), the oil diffuses from the wells to the surface of the composite, reducing adhesion. A few wells not fully emptied are outlined in yellow. Scale bar is 100 μm and applies to (F) and (G). Each data point and error bar are calculated from five different samples ($n = 5$).

obtained with standard commercial (3M Inc.) adhesive (Fig. 4F). Images of the skin of a healthy adult individual before and after wearing the adhesive (~8 hours) also show no induced redness or irritation (fig. S17). While the native adhesion and the influence of sweating are defined by the silicone adhesive layer (silicone gel 1) interfacing the composite and device with the body, experiments studying the effect of sweat on the adhesive function demonstrate that heavy sustained sweating (sauna at 60°C for 20 min) causes MA devices to fall off of the majority of individuals ($n = 3$).

Resistive heaters to wirelessly control thermally switchable adhesives

While these switchable adhesives can be activated by external means (e.g., heating pads), wireless modules that integrate directly into

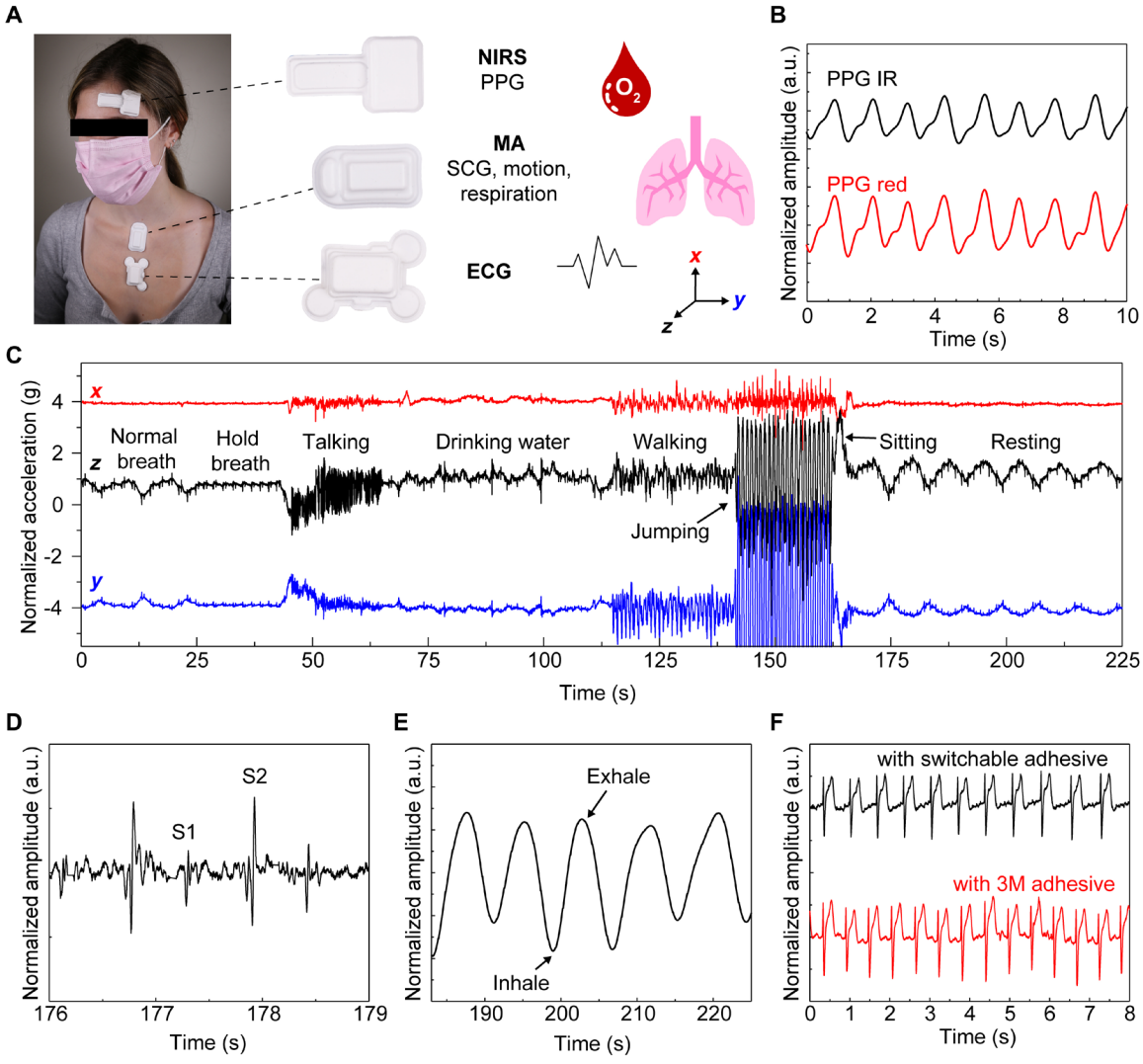

Fig. 4. Skin-interfaced wireless health-monitoring devices using thermally switchable adhesives (patterned oil well/silicone composites) to prevent skin injury during device removal. (**A**) NIRS, MA, and ECG devices worn at typical locations and schematic depictions of health signals that can be measured from each device. (**B**) A NIRS device mounted on the forehead with a thermally switchable adhesive yields photoplethysmogram (PPG) IR and PPG red signals. a.u., arbitrary units. (**C**) Three-axis accelerometry as representative MA data recorded over a 225-s interval and as an individual engages in various activities including drinking water, talking, walking, and resting. (**D** and **E**) Example of cardiac activity and respiration data from overall data in (C). (**F**) ECG waveforms measured using a thermally switchable adhesive and a standard commercial adhesive (2477P, 3M Inc.).

wearable devices provide a more convenient and more tightly controlled mode of operation. Figure 5 (A to C) highlights the design aspects of a compact circuit that supports this functionality, including the following main elements: (i) thermal actuating and sensing components, (ii) a Bluetooth low-energy system on a chip (BLE SoC) (nRF52832, Nordic Semiconductor) and associated antennas and crystals to digitize and transmit these data and support a two-way communication, (iii) power management–integrated components, and (iv) a flexible printed circuit board (fPCB) substrate to support and interconnect the components. The design adopts an island-bridge configuration, where the planar areas (islands) support electronic components connected through conductive traces, and the interconnects (bridges) localize bending strains away from the electronic components. The resistive heater material is a two-layer electrically conductive, flexible polyimide film (Kapton 200RS100, DuPont), with dimensions of ~20 mm by 25 mm for the examples presented here. Negative temperature coefficient (NTC) temperature sensors (one NTC coupled with the flexible heater and another reference NTC on the main board) enable real-time measurements of heater temperature. Closed loop control of the thermal actuator can be achieved by monitoring the temperature of the heater and modulating the power as needed. The temperature of the heater exhibits a linear relationship with applied power density; 0.2 W cm^{-2} achieves a temperature of 45°C across the heating area (Fig. 5D and fig. S16) after 200 s of actuation (Fig. 5E).

3D finite element analysis (FEA) yields distributions of temperature that qualitatively match those determined by IR imaging of the system on a skin replica (fig. S18). These models use properties associated with the system, such as dimensions, thermal conductivity (k), specific heat capacity (C_p), and density (ρ) (material properties

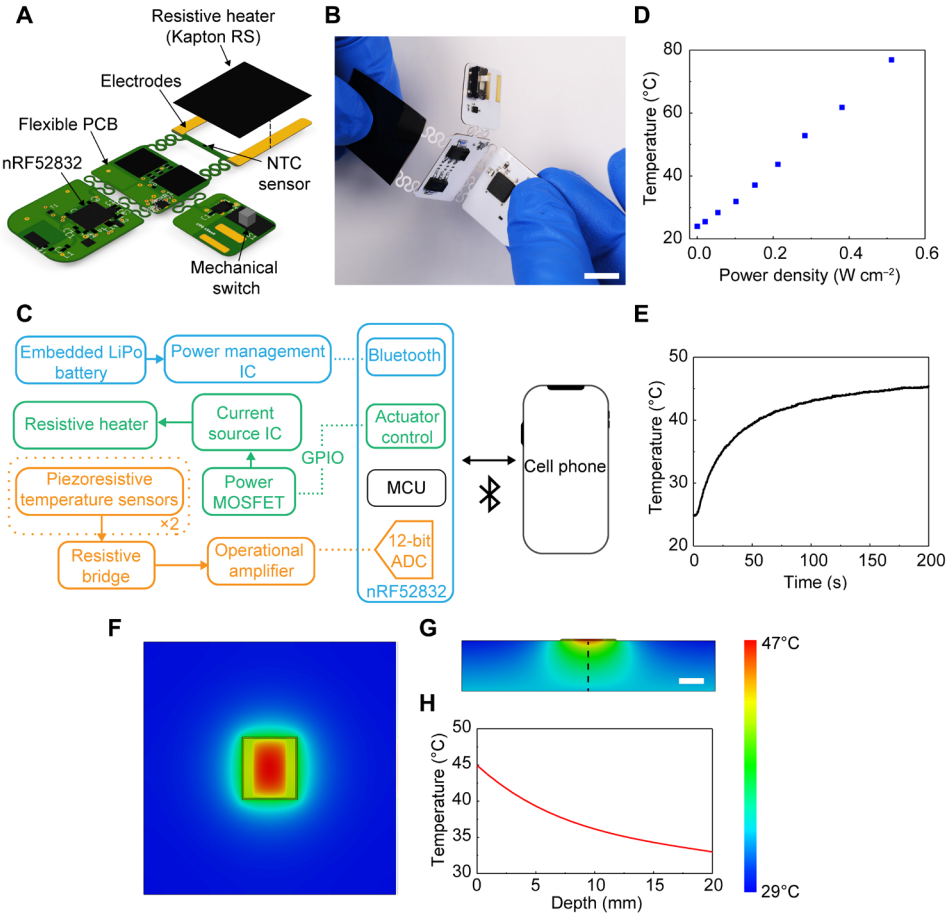

Fig. 5. Resistive heating circuit to wirelessly control adhesion. (**A**) Schematic illustration of the resistive heating circuit. (**B**) Image of a fabricated device during bending. Scale bar is 10 mm. (**C**) Schematic illustration of the electronic design for actuation, data acquisition, and wireless transmission. IC, integrated circuit. MOSFET, metal-oxide-semiconductor field-effect transistor. GPIO, general-purpose input/output. MCU, microcontroller unit. ADC, analog-to-digital converter. (**D**) Temperature versus power density for a resistive heater (Kapton 200RS100, DuPont) with a heating area of 14 mm by 24 mm (total area including contacts: 21 mm by 24 mm). (**E**) Temperature versus time at a power density of 0.2 W cm^{-1} for the system characterized in (D). (**F** and **G**) Temperature distribution at the surface of the skin (solid outline shows the area of the heater) (F) and in cross section of the skin (G) generated by 3D FEA. Linear color bar range is 29° to 47°C and applies to (F) and (G). Linear scale bar in (G) is 10 mm and applies to (F) and (G). (**H**) Temperature from 3D FEA simulation versus depth into the skin.

in table S3). Simulated FEA temperature distributions at the surface (Fig. 5F) and through the cross section (Fig. 5, G and H) of the skin show that the thermal exposure over the time period needed to achieve lowered adhesion (~260 s) is below guidelines even for infants.

Inserting this heating module directly within the MA device encapsulation yields a single, integrated system with wirelessly controlled adhesion to the skin (Fig. 6). The fPCB of the heating module folds around that for the MA (and is powered by the same battery) in a manner that only slightly increases the thickness and weight (1 mm taller and 1.3 g heavier) of the system, without changing the lateral dimensions (Fig. 6, B and C). The total energy required to trigger the release of the integrated heater and MA device is 190 J, compared to the 9990-J capacity of the battery. Placing this combined device at the suprasternal notch of a healthy adult individual (Fig. 6D) yields three-axis accelerometry measurements of the individual during a series of activities over 200 s (Fig. 6E). The extracted cardiac activity and respiration rate (fig. S19) confirm the quality of the data. After measurement, wirelessly activating the resistive heating circuit through a cell phone app allows the device to be removed in a low-adhesion state. This same integration strategy can be applied to the other devices in Fig. 4 after appropriate modifications to the geometry of the heating element.

DISCUSSION

This paper introduces materials and design concepts for switchable adhesives that can be implemented in skin-integrated device platforms to ensure safe and easy removal. A comprehensive set of experimental and modeling results define the effect of crystallizable oil type, loading, and organization within silicone matrices. Adhesion at the skin interface can be decreased by nearly a factor of three upon mild heating, thereby enabling devices to be removed with greatly reduced stresses on fragile skin. A low-profile, wirelessly controlled resistive heating module can be integrated directly into a range of skin-interfaced device platforms to enhance the convenience and to improve the precision control of the release process. The resulting materials and associated electronics technologies have most immediate applications across vulnerable patients in the NICU and PICU. Development of similarly switchable materials with electrical conductivity represents a direction for future work.

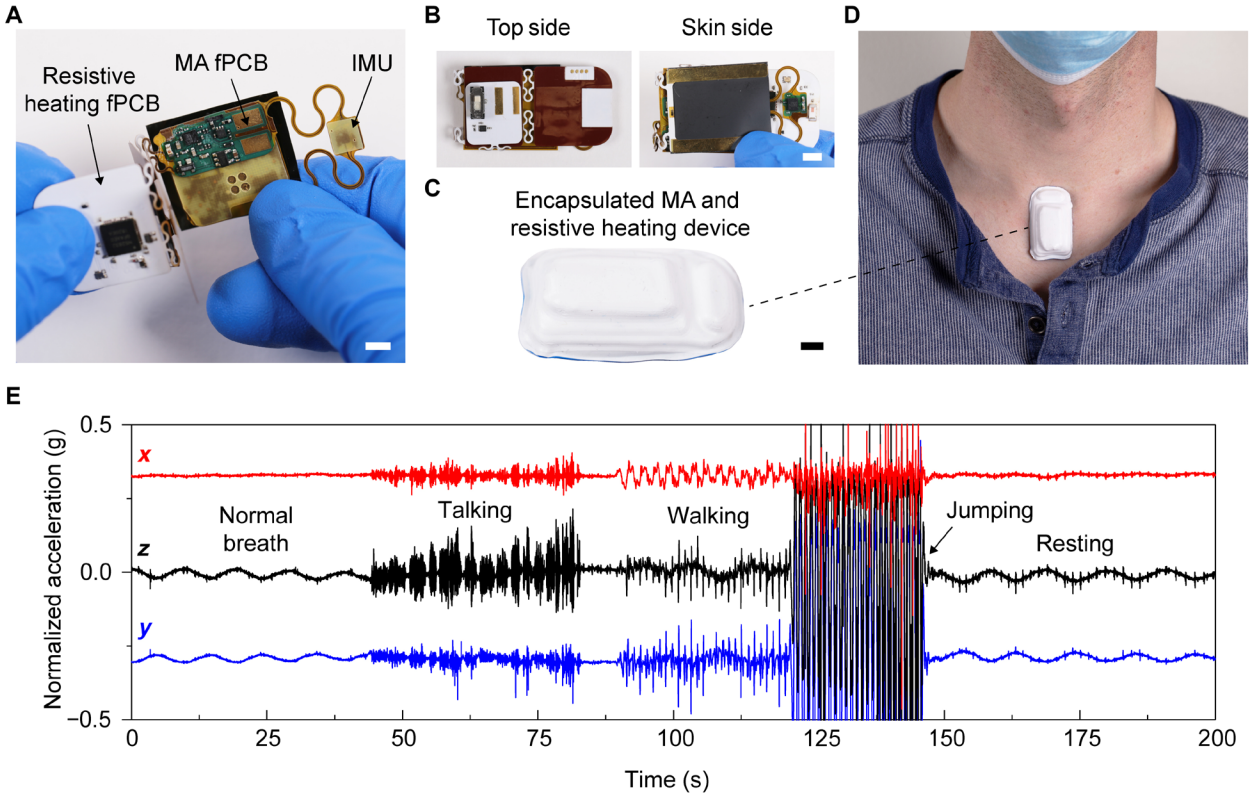

Fig. 6. Resistive heating circuit encapsulated with the MA device. (**A** to **C**) The resistive heating circuit folds around the MA device while still enabling data collection from the inertial measurement unit (IMU). Scale bars are 5 mm. (**D**) Device adhered at the suprasternal notch of a healthy adult. (**E**) Three-axis accelerometry from the MA device, measured over 200 s, while the individual performed different actions.

MATERIALS AND METHODS

Forming composites that consist of oil crystallites randomly distributed in silicone matrices

Mixing melted oils into preheated parts A/B of adhesive silicones (silicone gel 1: Ecoflex gel, Smooth-On or silicone gel 2: Silbione gel, Elkem Silicones) using a planetary mixer [ARE-310, THINKY Mixer; for 10 s at 2000 revolutions per minute (rpm)] and then spin coating at 500 to 800 rpm yielded uniform composites (~200 μm in thickness) of random oil crystallites suspended in an adhesive silicone matrix. Exposing the composites to ambient environment (23°C) for at least 2 hours cured the silicone. Spin coating the random crystallite composites with a thin film of silicone (silicone gel 1, 500 rpm) formed a skin-contacting adhesive layer on top of the composite (Fig. 2, D and E).

Forming silicon molds for deterministic composites

A 10-μm-thick layer of negative photoresist (KMPR 1010; spin cast at 3000 rpm for 30 s and soft baked at 110°C for 5 min), exposed to ultraviolet light (420 mJ cm^{-2}) through a Cr mask and then hard baked (110°C for 5 min) and developed (AZ 917MIF,; for 3 min) yielded patterns of resist. A deep reactive ion etch (DRIE) Bosch process (STS Pegasus ICP-DRIE, SPTS Technologies Ltd.) etched the exposed areas on the wafer to a depth of 15 μm.

Forming composites that consist of oil crystallites distributed in wells formed in silicone matrices

Spin-coating (250 rpm) polydimethylsiloxane (PDMS; Sylgard 184, Dow Corning) on the PDMS well mold, curing at 75°C for 30 min and then removing from the mold yielded silicone elements embossed with recessed wells. A discontinuous dewetting process (*42*, *43*) filled the wells with oil. Briefly, plasma treating (30 s) the wells followed by moving the liquid oil horizontally across the wells (24 mm min^{-1}) using a glass slide [treated with trichloro(1*H*,1*H*,2*H*,2*H*-perfluorooctyl) silane to produce a hydrophobic surface] suspended (1 mm) above the silicone surface (placed on a hot plate at elevated temperature to ensure the oil remained liquid) uniformly filled the wells with oil. After removing the sample from the hot plate to cool, spin coating a thin film of silicone (silicone gel 1, 500 rpm) formed a skin-contacting adhesive layer on top of the composite oil-filled wells.

Mechanical measurements

A modified T-peel test performed on a dynamic mechanical analyzer (RSA-G2, TA Instruments) quantified the adhesion energies between the adhesive composites and silicone skin replicas (Ecoflex 00-30; 10 mm in width, 20 mm in length, and 1 mm in thickness; shown in fig. S4). Laminating a layer (50 μm in thickness) of poly(L-lactic acid) (Goodfellow) on the back of the composites (10 mm in width, 20 mm in length, and 0.2 to 1 mm in thickness) eliminated elastic deformations during the measurements. An oven attached to the dynamic mechanical analyzer modulated the environmental temperature (held at temperature for 60 s before peeling). During peeling (rate = 0.5 mm s^{-1}), the dynamic mechanical analyzer software recorded the peel force as a function of displacement. Twice the saturated peel force divided by the sample width yields the adhesion energy (*40*, *41*). Mechanical tensile tests performed on a dynamic

mechanical analyzer (RSA-G2, TA Instruments) enabled stress versus strain measurements. The slope at low strain defined the elastic modulus.

Optical characterizations

High-resolution digital microscopes (VHX-1000, Keyence; Olympus 3D laser confocal microscope) optically characterized the oil/silicone composite morphologies. Confocal laser reflectance microscopy (Leica SP8) produced 3D images of oil/silicone composites. An ultraviolet-visible spectrophotometer (LAMBDA 1050, PerkinElmer) enabled optical transparency measurements of oil/silicone composites.

Thermal characterizations

The transient plane source (TPS) technique, discussed in more detail elsewhere (*47*, *48*), enabled measurements of thermal conductivity (k) of the silicone composites. Briefly, during TPS measurements, a resistive heating element applied heat on the surface of the sample. The transient temperature change, of either the heating element itself or of a separate temperature sensor, is simultaneously recorded.

Finite element analysis

The commercial software ABAQUS enabled 3D steady-state and transient heat transfer analysis to simulate the temperature distribution of the device. Eight-node linear heat transfer elements (DC3D8) were applied to all components. Air convection applied to the top surface of the skin and heater simulated the heat exchange with the surrounding environment. Using refined mesh in the model, especially the region around the heater, ensured calculation accuracy. The model consists of all parts of the device related to the transfer including resistive heater, electrodes, silicone, adhesive silicone gel layer, and skin. Table S3 summarizes the material properties used in all simulations. The thermal convection coefficient with air was 8 W m^{-2} K^{-1}, which was fitted with experiments on the skin replica (Sylgard 170). Applied power of 0.75 and 0.62 W were used for the simulations with and without PDMS and silicone gel 1, respectively.

Fabricating the resistive heating circuit

Commercial electronic design automation software (EAGLE version 9.6.1, Autodesk) generated the circuit schematic and design for the outsourced fPCBs. Multiple washes in deionized water and isopropanol (Thermo Fisher Scientific) removed surface oxides to prepare the fPCB for assembly. A nonconductive epoxy (Loctite 3621, Henkel) mechanically bonded the surface mount components to the fPCB, and reflow soldering (Weller WTHA1N, Weller Tools) with low-temperature solder paste (4900P SAC305, MG Chemicals) established electrical contact between surface mount components (microcontroller, amplifiers, dropout regulators, lithium polymer (LiPo) battery, tuning resistor, capacitors, inductors, and ceramic antennas) and the fPCB.

Human subject studies

For human subject studies, the studies were approved by the Northwestern University Institutional Review Board (STU00214661), Chicago, IL, USA and were registered on ClinicalTrials.gov. The individuals took part following the informed consent.

SUPPLEMENTARY MATERIALS

Supplementary material for this article is available at https://science.org/doi/10.1126/sciadv.abo0537

REFERENCES AND NOTES

1. O. Bonner, K. Beardsall, N. Crilly, J. Lasenby, "There were more wires than him": The potential for wireless patient monitoring in neonatal intensive care. *BMJ Innov.* **3**, 12–18 (2017).
2. C. Lund, Medical adhesives in the NICU. *Newborn Infant Nurs Rev* **14**, 160–165 (2014).
3. J. de Oliveira Marcatto, A. S. Santos, A. J. F. Oliveira, A. C. L. Costa, G. R. S. Regne, R. E. da Trindade, D. L. Couto, K. V. M. de Souza Noronha, M. V. Andrade, Medical adhesive-related skin injuries in the neonatology department of a teaching hospital. *Nurs. Crit. Care* , 10.1111/nicc.12621 (2021).
4. C. Konya, H. Sanada, J. Sugama, M. Okuwa, Y. Kamatani, G. Nakagami, K. Sakaki, Skin injuries caused by medical adhesive tape in older people and associated factors. *J. Clin. Nurs.* **19**, 1236–1242 (2010).
5. H. U. Chung, B. H. Kim, J. Y. Lee, J. Lee, Z. Xie, E. M. Ibler, K. Lee, A. Banks, J. Y. Jeong, J. Kim, C. Ogle, D. Grande, Y. Yu, H. Jang, P. Assem, D. Ryu, J. W. Kwak, M. Namkoong, J. B. Park, Y. Lee, D. H. Kim, A. Ryu, J. Jeong, K. You, B. Ji, Z. Liu, Q. Huo, X. Feng, Y. Deng, Y. Xu, K.-I. Jang, J. Kim, Y. Zhang, R. Ghaffari, C. M. Rand, M. Schau, A. Hamvas, D. E. Weese-Mayer, Y. Huang, S. M. Lee, C. H. Lee, N. R. Shanbhag, A. S. Paller, S. Xu, J. A. Rogers, Binodal, wireless epidermal electronic systems with in-sensor analytics for neonatal intensive care. *Science* **363**, eaau0780 (2019).
6. H. U. Chung, A. Y. Rwei, A. Hourlier-Fargette, S. Xu, K. Lee, E. C. Dunne, Z. Xie, C. Liu, A. Carlini, D. H. Kim, D. Ryu, E. Kulikova, J. Cao, I. C. Odland, K. B. Fields, B. Hopkins, A. Banks, C. Ogle, D. Grande, J. B. Park, J. Kim, M. Irie, H. Jang, J. Lee, Y. Park, J. Kim, H. H. Jo, H. Hahm, R. Avila, Y. Xu, M. Namkoong, J. W. Kwak, E. Suen, M. A. Paulus, R. J. Kim, B. V. Parsons, K. A. Human, S. S. Kim, M. Patel, W. Reuther, H. S. Kim, S. H. Lee, J. D. Leedle, Y. Yun, S. Rigali, T. Son, I. Jung, H. Arafa, V. R. Soundararajan, A. Ollech, A. Shukla, A. Bradley, M. Schau, C. M. Rand, L. E. Marsillio, Z. L. Harris, Y. Huang, A. Hamvas, A. S. Paller, D. E. Weese-Mayer, J. Y. Lee, J. A. Rogers, Skin-interfaced biosensors for advanced wireless physiological monitoring in neonatal and pediatric intensive-care units. *Nat. Med.* **26**, 418–429 (2020).
7. D.-G. Hwang, K. Trent, M. D. Bartlett, Kirigami-inspired structures for smart adhesion. *ACS Appl. Mater. Interfaces* **10**, 6747–6754 (2018).
8. H. E. Jeong, J.-K. Lee, H. N. Kim, S. H. Moon, K. Y. Suh, A nontransferring dry adhesive with hierarchical polymer nanohairs. *Proc. Natl. Acad. Sci.* **106**, 5639–5644 (2009).
9. D.-M. Drotlef, P. Blümler, A. del Campo, Magnetically actuated patterns for bioinspired reversible adhesion (dry and wet). *Adv. Mater.* **26**, 775–779 (2014).
10. E. Kizilkan, J. Strueben, A. Staubitz, S. N. Gorb, Bioinspired photocontrollable microstructured transport device. *Sci. Robot.* **2**, eaak9454 (2017).
11. J. W. Jeong, S. R. Yang, Y. H. Hur, S. W. Kim, K. M. Baek, S. Yim, H.-I. Jang, J. H. Park, S. Y. Lee, C.-O. Park, Y. S. Jung, High-resolution nanotransfer printing applicable to diverse surfaces via interface-targeted adhesion switching. *Nat. Commun.* **5**, 5387 (2014).
12. H. Yi, S. H. Lee, M. Seong, M. K. Kwak, H. E. Jeong, Bioinspired reversible hydrogel adhesives for wet and underwater surfaces. *J. Mater. Chem. B* **6**, 8064–8070 (2018).
13. S. Reddy, E. Arzt, A. del Campo, Bioinspired surfaces with switchable adhesion. *Adv. Mater.* **19**, 3833–3837 (2007).
14. H. Shahsavan, S. M. Salili, A. Jákli, B. Zhao, Thermally active liquid crystal network gripper mimicking the self-peeling of gecko toe pads. *Adv. Mater.* **29**, 1604021 (2017).
15. A. B. Croll, N. Hosseini, M. D. Bartlett, Switchable adhesives for multifunctional interfaces. *Adv. Mater. Technol.* **4**, 1900193 (2019).
16. S. S. Kwak, S. Yoo, R. Avila, H. U. Chung, H. Jeong, C. Liu, J. L. Vogl, J. Kim, H.-J. Yoon, Y. Park, H. Ryu, G. Lee, J. Kim, J. Koo, Y. S. Oh, S. Kim, S. Xu, Z. Zhao, Z. Xie, Y. Huang, J. A. Rogers, Skin-integrated devices with soft, holey architectures for wireless physiological monitoring, with applications in the neonatal intensive care unit. *Adv. Mater.* **33**, 2103974 (2021).
17. T. Oranges, V. Dini, M. Romanelli, Skin physiology of the neonate and infant: Clinical implications. *Adv. Wound Care* **4**, 587–595 (2015).
18. J. M. Dyer, R. A. Miller, Chronic skin fragility of aging: Current concepts in the pathogenesis, recognition, and management of dermatoporosis. *J. Clin. Aesthet. Dermatol.* **11**, 13–18 (2018).
19. "Standard guide for heated system surface conditions that produce contact burn injuries" (ASTM C1055-20, ASTM International, 2020).
20. A. R. Moritz, F. C. Henriques, Studies of thermal injury: II. The relative importance of time and surface temperature in the causation of cutaneous burns. *Am. J. Pathol.* **23**, 695–720 (1947).
21. R. R. Burch, Temperature switchable adhesives comprising a crystallizable oil, U.S. Patent 8828181B2 (2014).
22. W. Bierman, The temperature of the skin surface. *JAMA* **106**, 1158–1162 (1936).
23. M. A. Liebert, Final report on the safety assessment of cetearyl alcohol, cetyl alcohol, isostearyl alcohol, myristyl alcohol, and behenyl alcohol. *J. Am. Coll. Toxicol.* **7**, 359–413 (1988).
24. M. A. Liebert, Final report on the safety assessment of stearyl alcohol, oleyl alcohol, and octyl dodecanol. *J. Am. Coll. Toxicol.* **4**, 1–29 (1985).

25. "PubChem Compound Summary for CID 2682, 1-hexadecanol" (National Center for Biotechnology Information, 2022); https://pubchem.ncbi.nlm.nih.gov/compound/1-Hexadecanol.
26. B. E. Brown, W. Diembeck, U. Hoppe, P. M. Elias, Fate of topical hydrocarbons in the skin. *J. Soc. Cosmet. Chem.* **46**, 1–9 (1995).
27. Z. Jin, K. Wu, J. Hou, K. Yu, Y. Shen, S. Guo, A PTX/nitinol stent combination with temperature-responsive phase-change 1-hexadecanol for magnetocaloric drug delivery: Magnetocaloric drug release and esophagus tissue penetration. *Biomaterials* **153**, 49–58 (2018).
28. L. Tian, N. Gandra, S. Singamaneni, Monitoring controlled release of payload from gold nanocages using surface enhanced Raman scattering. *ACS Nano* **7**, 4252–4260 (2013).
29. P. C. H. Wong, P. W. S. Heng, L. W. Chan, Determination of solid state characteristics of spray-congealed ibuprofen solid lipid microparticles and their impact on sustaining drug release. *Mol. Pharm.* **12**, 1592–1604 (2015).
30. M. Maheshwari, A. R. Ketkar, B. Chauhan, V. B. Patil, A. R. Paradkar, Preparation and characterization of ibuprofen-cetyl alcohol beads by melt solidification technique: Effect of variables. *Int. J. Pharm.* **261**, 57–67 (2003).
31. J. Li, F. Zhang, Z. Hu, W. Song, G. Li, G. Liang, J. Zhou, K. Li, Y. Cao, Z. Luo, K. Cai, Drug "pent-up" in hollow magnetic prussian blue nanoparticles for NIR-induced chemo-photothermal tumor therapy with trimodal imaging. *Adv. Healthc. Mater.* **6**, 1700005 (2017).
32. C. Cao, N. Yang, H. Dai, H. Huang, X. Song, Q. Zhang, X. Dong, Recent advances in phase change material based nanoplatforms for cancer therapy. *Nanoscale Adv.* **3**, 106–122 (2021).
33. S. Becherini, M. Mitmoen, C. D. Tran, Biocompatible and smart composites from cellulose, wool, and phase-change materials encapsulated in natural sporopollenin microcapsules. *ACS Sustain. Chem. Eng.* **8**, 10089–10101 (2020).
34. C. Pisani, E. Rascol, C. Dorandeu, C. Charnay, Y. Guari, J. Chopineau, J.-M. Devoisselle, O. Prat, Biocompatibility assessment of functionalized magnetic mesoporous silica nanoparticles in human HepaRG cells. *Nanotoxicology* **11**, 871–890 (2017).
35. L. Che Rose, J. C. Bear, P. D. McNaughter, P. Southern, R. B. Piggott, I. P. Parkin, S. Qi, A. G. Mayes, A SPION-eicosane protective coating for water soluble capsules: Evidence for on-demand drug release triggered by magnetic hyperthermia. *Sci. Rep.* **6**, 20271 (2016).
36. C. C. Ng, Y.-L. Cheng, B. A. Saville, Thermoresponsive polymer membrane for the local delivery of drugs. *Sex Reprod. Med.* **1**, 21–27 (2001).
37. L. Liu, K. Kuffel, D. K. Scott, G. Constantinescu, H.-J. Chung, J. Rieger, Silicone-based adhesives for long-term skin application: Cleaning protocols and their effect on peel strength. *Biomed. Phys. Eng. Express.* **4**, 015004 (2018).
38. R. Herbert, J.-H. Kim, Y. S. Kim, H. M. Lee, W.-H. Yeo, Soft material-enabled, flexible hybrid electronics for medicine, healthcare, and human-machine interfaces. *Materials* **11**, 187 (2018).
39. J. M. Silva, C. V. Pereira, F. Mano, E. Silva, I. Sa, R. L. Reis, A. Paiva, A. A. Matias, A. R. C. Duarte, Therapeutic role of deep eutectic solvents based on menthol and saturated fatty acids on wound healing. *ACS Appl. Bio Mater.* **2**, 4346–4355 (2019).
40. R. S. Rivlin, A. G. Thomas, Rupture of rubber. I. Characteristic energy for tearing. *J. Polym. Sci.* **10**, 291–318 (1953).
41. J. Yang, R. Bai, Z. Suo, Topological adhesion of wet materials. *Adv. Mater.* **30**, 1800671 (2018).
42. R. J. Jackman, D. C. Duffy, E. Ostuni, N. D. Willmore, G. M. Whitesides, Fabricating large arrays of microwells with arbitrary dimensions and filling them using discontinuous dewetting. *Anal. Chem.* **70**, 2280–2287 (1998).
43. H. U. Kim, Y. H. Roh, S. J. Mun, K. W. Bong, Discontinuous dewetting in a degassed mold for fabrication of homogeneous polymeric microparticles. *ACS Appl. Mater. Interfaces* **12**, 53318–53327 (2020).
44. A. Y. Rwei, W. Lu, C. Wu, K. Human, E. Suen, D. Franklin, M. Fabiani, G. Gratton, Z. Xie, Y. Deng, S. S. Kwak, L. Li, C. Gu, A. Liu, C. M. Rand, T. M. Stewart, Y. Huang, D. E. Weese-Mayer, J. A. Rogers, A wireless, skin-interfaced biosensor for cerebral hemodynamic monitoring in pediatric care. *Proc. Natl. Acad. Sci. U.S.A.* **117**, 31674–31684 (2020).
45. K. Lee, X. Ni, J. Y. Lee, H. Arafa, D. J. Pe, S. Xu, R. Avila, M. Irie, J. H. Lee, R. L. Easterlin, D. H. Kim, H. U. Chung, O. O. Olabisi, S. Getaneh, E. Chung, M. Hill, J. Bell, H. Jang, C. Liu, J. B. Park, J. Kim, S. B. Kim, S. Mehta, M. Pharr, A. Tzavelis, J. T. Reeder, I. Huang, Y. Deng, Z. Xie, C. R. Davies, Y. Huang, J. A. Rogers, Mechano-acoustic sensing of physiological processes and body motions via a soft wireless device placed at the suprasternal notch. *Nat. Biomed. Eng.* **4**, 148–158 (2020).
46. H. Jeong, J. Y. Lee, K. Lee, Y. J. Kang, J.-T. Kim, R. Avila, A. Tzavelis, J. Kim, H. Ryu, S. S. Kwak, J. U. Kim, A. Banks, H. Jang, J.-K. Chang, S. Li, C. K. Mummidisetty, Y. Park, S. Nappi, K. S. Chun, Y. J. Lee, K. Kwon, X. Ni, H. U. Chung, H. Luan, J.-H. Kim, C. Wu, S. Xu, A. Banks, A. Jayaraman, Y. Huang, J. A. Rogers, Differential cardiopulmonary monitoring system for artifact-canceled physiological tracking of athletes, workers, and COVID-19 patients. *Sci. Adv.* **7**, eabg3092 (2021).
47. S. E. Gustafsson, Transient plane source techniques for thermal conductivity and thermal diffusivity measurements of solid materials. *Rev. Sci. Instrum.* **62**, 797–804 (1991).
48. S. R. Madhvapathy, H. Wang, J. Kong, M. Zhang, J. Y. Lee, J. B. Park, H. Jang, Z. Xie, J. Cao, R. Avila, C. Wei, V. D'Angelo, J. Zhu, H. U. Chung, S. Coughlin, M. Patel, J. Winograd, J. Lim, A. Banks, S. Xu, Y. Huang, J. A. Rogers, Reliable, low-cost, fully integrated hydration sensors for monitoring and diagnosis of inflammatory skin diseases in any environment. *Sci. Adv.* **6**, eabd7146 (2020).
49. A. Bellili, N. David, B. Vandame, Q. Wang, Y. Goutille, E. Richaud, Diffusion and solubility of mineral oils through ethylene-vinyl acetate copolymer. *Polym. Test.* **31**, 236–247 (2012).
50. J. N. Lee, C. Park, G. M. Whitesides, Solvent compatibility of poly(dimethylsiloxane)-based microfluidic devices. *Anal. Chem.* **75**, 6544–6554 (2003).
51. S. C. George, S. Thomas, K. N. Ninan, Molecular transport of aromatic hydrocarbons through crosslinked styrene-butadiene rubber membranes. *Polymer* **37**, 5839–5848 (1996).
52. A. Joseph, A. E. Mathai, S. Thomas, Sorption and diffusion of methyl substituted benzenes through cross-linked nitrile rubber/poly(ethylene co-vinyl acetate) blend membranes. *J. Membr. Sci.* **220**, 13–30 (2003).
53. J. Crank, *The Mathematics of Diffusion* (Clarendon Press, ed. 2, 1975).
54. G. Liu, M. Cai, Y. Feng, X. Wang, F. Zhou, W. Liu, Photothermally actuated interfacial hydration for fast friction switch on hydrophilic polymer brush modified PDMS sheet incorporated with Fe_3O_4 nanoparticles. *Chem. Commun.* **52**, 3681–3683 (2016).

Acknowledgments

Funding: This work made use of the NUFAB facility of Northwestern University's NUANCE Center, which has received support from the SHyNE Resource (NSF ECCS-2025633), the IIN, and Northwestern's MRSEC program (NSF DMR-1720139). 3D microscopy was performed at the Biological Imaging Facility at Northwestern University (RRID: SCR_017767), supported by the Chemistry of Life Processes Institute, the NU Office for Research, the Department of Molecular Biosciences, and the Rice Foundation. This work also made use of the MatCI Facility supported by the MRSEC program of the NSF (DMR-1720139) at the Materials Research Center of Northwestern University. S.L. acknowledges support from the Ryan Fellowship and the International Institute for Nanotechnology at Northwestern University. H.A. acknowledges support from the National Institute of Neurological Disorders and Stroke of the National Institutes of Health (award no. F31NS115422). E.C. acknowledges support from Northwestern University through a Summer Undergraduate Research Grant. **Author contributions:** Conceptualization: K.R.J. and J.A.R. Methodology: K.R.J., S.L., H.A., H.J., C.W., X.N., and D.C. Investigation: K.R.J., S.L., H.A., H.J., Y.J.L., C.W., and E.C. Supervision: Y.H. and J.A.R. Manuscript preparation was led by K.R.J. and J.A.R., with contributions from all authors. **Competing interests:** J.A.R. is a co-founder and board member of Sibel Health, a company that is commercializing vital signs measurement systems. The authors declare that they have no other competing interests. **Data and materials availability:** All data needed to evaluate the conclusions in the paper are present in the paper and/or the Supplementary Materials.

Submitted 11 January 2022
Accepted 27 April 2022
Published 10 June 2022
10.1126/sciadv.abo0537